Acoustic metamaterial for low frequency sound absorption in linear and nonlinear regimes

Daniel C. Brooke, Olga Umnova, Philippe Leclaire, Thomas Dupont

Journal of Sound and Vibration 485 (2020) 115585

Contents lists available at ScienceDirect

Journal of Sound and Vibration

journal homepage: www.elsevier.com/locate/jsv

Acoustic metamaterial for low frequency sound absorption in linear and nonlinear regimes

Daniel C. Brooke[a,*], Olga Umnova[a], Philippe Leclaire[b], Thomas Dupont[c]

[a] University of Salford, Manchester, England, UK
[b] DRIVE – ISAT Universitie de Bourgogne, Nevers, France
[c] Ecole de Technologie Superieure (ETS) – Universitie du Quebec, Montreal, Canada

ARTICLE INFO

Article history:
Received 20 March 2020
Revised 12 July 2020
Accepted 14 July 2020
Available online 16 July 2020

Keywords:
Acoustic metamaterials
Dead-end pores
Low frequency
Sound absorption
Nonlinear regime
Forchheimer's nonlinearity

ABSTRACT

Acoustic metamaterial absorbers have been built and tested with focus on low frequency airborne sound absorption in linear and nonlinear regimes. The absorbers are made up of a series of piled up flat cavities, separated by thin walls and traversed by a perforation at their centre. A model for absorber effective properties is developed and compared with experimental data. The model is used to derive simple formulae for the frequency and the peak value of the absorption coefficient at the lowest frequency resonance, depending on the geometrical parameters of the structure. Different absorbers have been built with several cavity thicknesses to allow comprehensive comparisons with the model. Nonlinear properties of the absorbers are investigated experimentally using sine wave excitation around the resonance frequency with the amplitude of the incident wave up to 250 Pa. Flow resistivity measurements at low flow rates show that the periodic set of cavities does not modify resistivity significantly when compared to a simple perforated cylinder with same thickness. As flow rate increases, the flow resistivity grows linearly according to Forchheimer's law and has a significant dependence on the absorber thickness. A numerical model is developed accounting for the linear growth of flow resistivity with particle velocity amplitude in the central perforation and compared with the measurements at high amplitudes of the incident wave.

List of symbols

ω	angular sound frequency
p	pressure of sound wave
v	particle velocity of sound wave
c	sound speed in air
ρ_0	density of air
η	viscosity of air
$C_0 = \frac{1}{\rho_0 c^2}$	compressibility of air
$k = \frac{\omega}{c}$	wavenumber of air

* Corresponding author.
E-mail addresses: D.C.Brooke@edu.salford.ac.uk (D.C. Brooke), O.Umnova@edu.salford.ac.uk (O. Umnova), Philippe.Leclaire@u-bourgogne.fr (P. Leclaire), Thomas.Dupont@etsmtl.ca (T. Dupont).

https://doi.org/10.1016/j.jsv.2020.115585
0022-460X/

N_{pr}	Prandtl number
γ	adiabatic constant
Re	Reynolds number
R	outer radius of the absorber
r_0	radius of central perforation
d_p	plate thickness
d_c	width of lateral cavity (distance between the plates)
L	absorber thickness
$\rho(\omega), C(\omega)$	effective density and effective compressibility of air inside the perforation with the lateral cavities
$\rho_p(\omega), C_p(\omega)$	effective density and effective compressibility of air inside the main perforation without lateral cavities
$\rho_c(\omega), C_c(\omega)$	effective density and effective compressibility of air inside the lateral cavities
$k_c = \omega\sqrt{C_c(\omega)\rho_c(\omega)}$	wavenumber of air in the lateral cavity
$q = \omega\sqrt{\rho(\omega)C(\omega)}$	wavenumber of air inside the absorber
$\phi_p = (\frac{r_0}{R})^2$	surface porosity of the absorber
$\phi_w = \frac{d_c}{d_c+d_p}$	porosity of the main perforation wall
ξ	Forchheimer's nonlinearity parameter
V_f	flow velocity in the flow resistivity rig tube
$U = \frac{V_f}{\phi_p}$	flow velocity in the main perforation
$\sigma_{p,\,c}, \sigma$	static flow resistivity of the main perforation, cavity and the whole sample, respectively
$\Lambda_{\mathrm{p,\,c}}$	characteristic viscous length for the main perforation and cavity, respectively
$\alpha_{\infty p,\,c}$	high frequency tortuosity for the main perforation and cavity, respectively
$\kappa'_{p,c}$	thermal permeability for the main perforation and cavity, respectively
$\Lambda'_{p,c}$	thermal characteristic length for the main perforation and cavity, respectively
f_r	frequency of the first absorber resonance
α_r	peak value of the absorption coefficent at resonance
p_i	incident pressure amplitude

1. Introduction

In recent work by Dupont et al., [1], a 3D printed microstructure was considered that contains a periodic arrangement of thin plates with central perforation separated by cavities (Fig. 1), the so-called "pancake absorber". This absorber is one of the realizations of the microstructure design suggested earlier in work by Leclaire et al [2] where the additional laterally arranged pores are coupled with the main perforation. Low value of sound speed through the perforation achieved in these structures [3] leads to the existence of the absorption peaks at low frequencies. In [1], a transfer matrix model (TMM) is used to predict the frequency dependence of the absorption coefficient, which gives a good agreement with the measurements. The pancake absorbers are proven to be effective for low frequency sound absorption at only a few centimetres in thickness.

Metamaterial structures, studied in this work, are similar to pancake absorbers (and for this reason we use the same name) but made of periodically arranged metallic plates with the central perforation. They are mechanically robust and do not contain any fibrous materials or foams. This makes them good candidates, alongside with microperforated absorbers, for the use in hostile environments for attenuation of high amplitude noise [4]. It is known that the dominating nonlinearity in

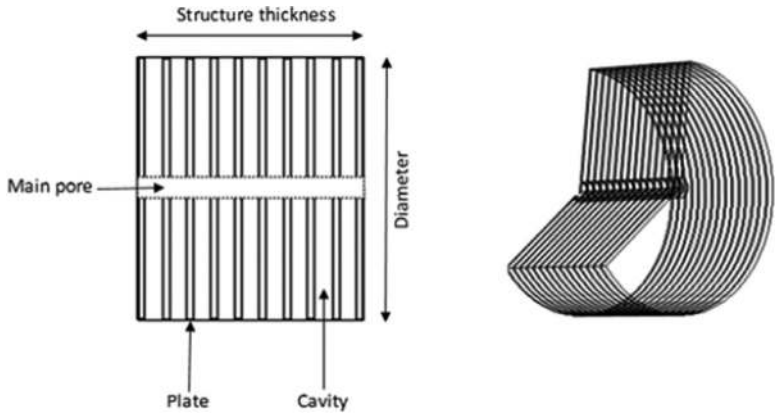

Fig. 1. Geometry of the sample.

rigid porous materials is of Forchheimer's type, associated with the growth of static flow resistivity with the Reynold's number (and consequently pressure amplitude). It was noted by Kuntz and Blackstock, [5] that although the usual manifestation of acoustic nonlinearity in fluids is harmonics generation, this does not happen in porous materials where the losses are high. Instead, the losses themselves become amplitude dependent. In the last three decades, the Forchheimer's nonlinearity in rigid porous materials has been studied in numerous papers, see for instance [6–13]. Numerical and analytical models have been developed, based on modifications of the effective material density to include particle velocity dependence of flow resistivity, and sucessfully compared with the data.

Nonlinear behaviour of absorbers with low surface porosity, single orifices and micro perforated plates (MPP), has been studied extensively starting from a pioneering work by Sivian [14]. Ingard and Ising [15] measured acoustic resistance and reactance of an orifice as a function of velocity amplitude in it, demonstrating strong nonlinearity of acoustic resistance and lower effect of velocity on acoustic reactance. The high values of particle velocity reached at the perforation lead to the formation of vortices, which, in turn, affect the acoustic resistance. The acoustic nonlinearity of orifices have then been studied both theoretically and experimentally by Cummings and co authors. In [16] the model was developed for the sound transmission through the duct termination at high amplitudes in the presence and in the absence of steady flow. It was compared with the data obtained using broadband signals, and a good agreement has been demonstrated. The model was then validated for tone bursts by measuring transmission coefficent through the orifice at different sound pressure levels [17]. The vortices, generated at both sides of the orifice, have been visualised and their translational velocity measured for different peak velocities inside the orifices. A good agreement of the frequency domain model with both high amplitude broadband signals and tone bursts can be considered as a confirmation that in the case of strong nonlinear losses, the interactions between different frequency components is weak and Fourier transform could still provide useful results. The simple model accounting for the nonlinear resistance of the orifice, has been recently used in work of Achilleos et al [18] to study the nonlinearity of Helmholtz resonators, side loaded to the waveguide. It has been shown that, due to the increase of resistance with incident pressure amplitude, the initially low peak absorption of Helmholtz resonator increases and reaches the unity at 160 dB. Nonlinearities in microperforated panel (MPP) absorbers have first been studied by Maa in [19] The resistance of the orifice has been expressed as a linear function of the Mach number inside it and of the open area (equivalent to front surface porosity). The weak nonlinearity of the acoustic reactance of the orifice has also been accounted for. A more precise, empirical model for the nonlinear resistance has been proposed in [4] based on the data obtained for SPL around 140 dB, characteristic for launcher fairings applications. Tayong et al in [20] studied the dependence of the peak absorption of the MPP backed by air cavity, both theoretically and numerically. It has been demonstrated that the peak absorption coefficient can grow up to a maximum value of 1 as Mach number increases to a critical value, similar results were obtained for Helmholtz resonators in [18]. When the Mach number is higher than the critical value, the absorption decreases with it. In subsequent work [21] by Tayong et al the interaction between the multiple holes in MPP in the nonlinear regime has been studied experimentally. The model which treats the nonlinearity of the MPP absorber using equivalent fluid approach [22] was developed by Laly et al in [23]. They have shown that the nonlinear correction to the acoustic resistance of MPP expressed as a linear function of velocity can be interpreted in terms of velocity dependent flow resistivity of the plate, i.e. Forchheimer's nonlinearity. Unlike rigid porous material models, they also considered velocity dependence of the tortuosity due to nonlinear decrease of the end correction.

The pancake absorbers are different from conventional porous materials in two respects. First, the surface porosity, defined as the ratio of the main perforation surface area to the front surface area of the absorber, is much lower than that of a conventional porous absorber. This means the early onset of nonlinearity, due to large values of Reynolds number inside the main perforation, similar to MPP absorbers. However, contrary to MPPs, these absorber thickness is much larger than the size of the perforation. The latter means that the models should account for sound propagation within the structure. A simple approximation of the surface impedance assuming that the wavelength is much larger than the thickness of the sample, used for instance in [24], might not be valid.

Second difference with the conventional rigid porous materials is the particular microstructure of the absorber. The presence of the lateral cavities makes it effectively a double porosity structure as described by Olny and Boutin in [25] with the first porosity scale associated with the main perforation and the second with the lateral cavities. The interaction of high amplitude sound with double porosity materials is a new topic to be studied.

The paper is organised as follows. In Section 2, we start with developing a linear model for the effective properties, density and bulk modulus, of the absorber and use it to predict the dependence of the position of the lowest resonance frequency and the peak value of the absorption coefficient on the structure geometry. For these, we derive simple analytical approximations. This model is validated against the experimental results obtained in standard impedance tube using white noise excitation. The measurements have been done on several samples, with different thicknesses and cavity widths, to investigate the limitations of the model. In Section 3, the measurements of flow resistivity of the samples are described. These measurements are necessary to obtain the Forchheimer'sparameters, to be used in the nonlinear model. To investigate the effect of lateral cavities on the static flow resistivity values and on Forchheimer's nonlinearity parameter, the measurements performed on several absorbers and also on the corresponding solid cylinders with same thickness and central perforation size (thus eliminating the effect of cavities completely). The samples of different thicknesses have been tested in flow resistivity rig too. In Section 4, the nonlinear model is described and validated using pure tone signals of different amplitudes. The model does not have any adjustable parameters and uses independently measured Forchheimer's nonlinearity parameters, as described in Section 3. The absorption coefficient measurements are performed in specially designed high

sound pressure level (HSPL) impedance tube. The highest-pressure level of the incident wave achieved in the tube is around 160 dB. The Conclusions summarise the main results of the work.

2. Absorber in the linear regime – model and its experimental validation

2.1. Model

2.1.1. Effective properties

We consider an absorber composed of equally spaced identical rigid plates with radius R and thickness d_p, where subscript "p" stands for "plate". Each plate has a central perforation with radius r_0. The spacing between the plates is d_c, where subscript "c" stands for "cavity". The cavities are rigidly backed at the outer boundary, R. The geometry is shown in Fig. 1.

To obtain effective properties of the structure, the results derived in a previous publication [2] will represent a starting point for establishing the model adapted to the new geometry. In the current design, periodically spaced cylindrical dead end (subscript "de") pores, as they are referred in [2], are replaced by the annular cavities with the outer radius R, inner radius r_0 and thickness d_c. Low frequency approximation is considered, meaning that wavelength of sound travelling through the main perforation is much larger than the period of the structure, $Re(k_{mp}h) \ll 1$. Here subscript mp stands for "main perforation", k_{mp} is wavenumber of air in the main perforation without cavities present and $h = d_p + d_c$ is the period of the structure. Expressions for the characteristic impedance Z and wavenumber q of air in the pore with the dead ends present are given by Eqs. (28) and (32) in [2]:

$$Z = \frac{Z_{mp}}{\sqrt{1 + \frac{2X}{ik_{mp}h}}} \tag{1}$$

$$q = k_{mp}\sqrt{1 + \frac{2X}{ik_{mp}h}} \tag{2}$$

where time convention is $e^{-i\omega t}$.

Parameter X is defined by Eq. (2) in [2]

$$X = -\frac{NA_{de}}{2\ A_{mp}}\frac{1}{Z_{s\ de}} \tag{3}$$

here N is the number of dead end pores per period, A_{mp} is the cross sectional area of the main pore and A_{de} is the cross section area of the dead end pore opening into the main pore. $Z_{s\,de}$ is the surface (hence subscript "s") impedance of the single dead end pore normalised to the characteristic impedance of air in the main pore, Z_{mp}. For the current design, NA_{de}, which is the total surface area of the cavity opening into the main perforation per period, is equal to $2\pi r_0 d_c$ (therefore $NA_{de} \rightarrow 2\pi r_0 d_c$). The surface area of the main cylindrical perforation is πr_0^2 (therefore $A_{mp} \rightarrow \pi r_0^2$). Introducing surface admittance of the cavity normalised by the characteristic admittance of air $\frac{1}{\rho_0 c}$, $G(\omega) = \frac{\rho_0 c}{Z_{s\ de}\ Z_{mp}}$, Eq. (3) can be rewritten as

$$X = -\frac{1}{\rho_0 c}\frac{d_c}{r_0}\ G(\omega)\ Z_{mp}. \tag{4}$$

Now expressions for the effective density $\rho(\omega)$ and effective compressibility $C(\omega)$ of air within the perforation with the side cavities can be derived from (1), (2) and (4). Note that to reflect the change in geometry, the subscript p is now used for the quantities related to "perforation" ($mp \rightarrow p$) and subscript c is used for the quantities related to "cavity" ($de \rightarrow c$):

$$\rho(\ \omega) = \frac{qZ}{\omega} = \rho_p, \tag{5}$$

$$C(\ \omega) = \frac{q}{\omega Z} = C_p + iC_0\frac{2}{kr_0}\ G_w(\omega), \tag{6}$$

where $k = \frac{\omega}{c}$ is wavenumber of air, $C_0 = \frac{1}{\rho_0 c^2}$ is compressibility of air, the admittance of the main perforation wall is $G_w(\omega) = G(\omega)$, $\phi_w = \frac{\rho_0 c}{Z_{s\ c}\ Z_p}\phi_w$ and $\phi_w = \frac{d_c}{h}$ can be treated as porosity of the main perforation wall. It follows from Eq. (5) that the presence of the lateral cavities does not affect the effective density of air in the main perforation and it remains equal to that of the perforation without the cavities $\rho_p = \frac{Z_p k_p}{\omega}$. The effective compressibility of air inside the structure is not equal to that of the perforation, $C_p = \frac{k_p}{\omega Z_p}$, and is dependent of the geometry of the cavities.

Surface impedance of the perforation wall $G_w(\omega)$ is calculated assuming no angular dependence of pressure inside the cavities so that it varies only with the polar coordinate r, which is defined as the distance from the centre of the main pore. Helmholz equation for pressure inside the cavity in this case is

$$p'' + \frac{1}{r}p' + k_c^2 p = 0, \tag{7}$$

Table 1
Parameters of JCAL model for the perforation and the cavities [27].

Parameter	Perforation (subscript p)	Cavity (subscript c)
$\sigma_{p,\,c}$	$8\eta/r_0^2$	$12\eta/d_c^2$
$\alpha_{\infty\,p,\,c}$	1	1
$\Lambda_{p,\,c}$	r_0	d_c
$\Lambda'_{p,c}$	r_0	d_c
$\kappa'_{p,c}$	$r_0^2/8$	$d_c^2/12$
$\omega_{b\;p,c} = \omega'_{b\;p,c}$	$16\eta/\rho_0\; r_0^2$	$36\eta/\rho_0\; d_c^2$

where $k_c(\omega)$ is effective wavenumber of air in the cavity of thickness d_c between two rigid plates. The derivatives are with respect to r.

Relationship between the radial component of particle velocity $v(r)$ and pressure $p(r)$ in the fluid with effective density $\rho_c(\omega)$ is followed from the Euler's equation

$$v = \frac{-ip'}{\omega\rho_c(\omega)}. \tag{8}$$

General solution of Eq. (7) can be written as $p = A\,J_0(k_c r) + BH_0(k_c r)$, where J_0 and H_0 are Bessel function and Hankel function of the first kind respectively, A and B are arbitrary constants. The cavity is rigidly backed at $r = R$, so boundary condition $p'(R) = 0$ is applied. This results in the following expression for pressure and particle velocity in the cavity

$$p = A\left(J_0(k_c r) - \frac{J_1(k_c R)}{H_1(k_c R)}H_0(k_c r)\right) \tag{9}$$

$$v = \frac{iAk_c}{\omega\rho_c}\left(J_1(k_c r) - \frac{J_1(k_c R)}{H_1(k_c R)}H_1(k_c r)\right) \tag{10}$$

Normalised surface admittance of the wall of the main perforation is calculated as $G_w = \rho_0 c\phi_w \frac{v(r_0)}{p(r_0)}$ giving

$$G_w = \frac{i\;\phi_w\rho_0 c}{Z_c}\frac{\left(J_1(k_c r_0) - \frac{J_1(k_c R)}{H_1(k_c R)}H_1(k_c r_0)\right)}{\left(J_0(k_c r_0) - \frac{J_1(k_c R)}{H_1(k_c R)}H_0(k_c r_0)\right)} \tag{11}$$

where $Z_c(\omega) = \sqrt{\frac{\rho_c(\omega)}{C_c(\omega)}}$ is characteristic impedance of air in the cavity.

The model for the effective properties of air inside the structure, $\rho(\omega)$ and $C(\omega)$, defined by Eqs. (5), (6) and (11) can be used to calculate the surface impedance Z_s of the absorber and its absorption coefficient α using the usual expressions. In case of rigidly backed absorber of thickness L they are

$$Z_s = i\frac{Z}{\phi_p}\;\mathrm{cotan}(qL), \tag{12}$$

$$\alpha = 1 - \left|\frac{Z_s - \rho_0 c}{Z_s + \rho_0 c}\right|^2, \tag{13}$$

with $\phi_p = (\frac{r_0}{R})^2$ being the front surface porosity, $Z = \sqrt{\frac{\rho(\omega)}{C(\omega)}}$, $q(\omega) = \omega\sqrt{\rho(\omega)C(\omega)}$.

For further calculations, expressions for effective density and compressibility of air in straight cylindrical pore and in the cavity, i.e. slit with thickness d_c, $\rho_{p,c}(\omega)$ and $C_{p,c}(\omega)$, are required. These are obtained using Johnson-Champoux -Allard -Lafarge (JCAL) equivalent fluid model [22,26,27]:

$$\rho_{p,\;c}(\omega) = \rho_0\;\alpha_{\infty\;p,c}\left(1 + \frac{\sigma_{p,c}}{-i\omega\alpha_{\infty\;p,c}\rho_0}\sqrt{1 + \frac{-i\omega}{\omega_{b\;p,c}}}\right) \tag{14}$$

$$C_{p,\;c}(\omega) = C_0\left(\gamma - \frac{\gamma - 1}{1 + \frac{\eta}{-i\omega'\rho_0\kappa'_{p,c}}\sqrt{1 + \frac{-i\omega'}{\omega'_{b\;p,c}}}}\right) \tag{15}$$

where $\omega' = \omega N_{pr}$, N_{pr} is Prandtl number, $\omega_{b\;p,c} = \frac{\sigma_{p,c}^2\Lambda_{\;p,c}^{\;2}}{4\,\alpha_{\infty\;p,c}^2\,\rho_0\eta}$ and $\omega'_{b\;p,c} = \frac{\Lambda'^{\;2}_{\;p,c}\eta}{4\,\kappa'^2_{pc}\rho_0}$ are characteristic viscous and thermal frequencies of the main pore (p) and lateral cavities (c). The parameters of the model, static air flow resistivity σ, characteristic viscous length Λ, high frequency tortuosity α_∞, thermal permeability κ' and thermal characteristic length Λ' can be calculated using simple expressions (given in Table 1) for the central perforation (straight cylindrical pore of radius r_0) and for the cavity (slit of thickness d_c).

The model described in this section will be further referred to as "full model". It is applicable when the wavelength of sound propagating through the structure is much larger than the period of the microstructure, i.e. $Re(q)h \ll 1$.

2.1.2. Estimation of resonance frequency f_r *and absorption coefficient* α_r *at first resonance*

To estimate the frequency of the first resonance f_r of the hard-backed layer with thickness L the following assumptions are used. First, it is assumed that

$$|k_c(2\pi f_r)|R \ll 1 \tag{16}$$

which allows to use Bessel functions' expansions for small arguments. This assumption means that at resonance the wavelength of sound within the lateral cavities is much larger than their radius R. Second, resonance frequency is assumed to be much higher than characteristic viscous and thermal frequencies for both main perforation and lateral cavities, $f_r \gg f_{b\ p,c} = \frac{\omega_{b\ p,c}}{2\pi}$ and $f_r \gg f'_{b\ p,c} = \frac{\omega'_{b\ p,c}}{2\pi}$. Using expressions for JCAL model parameters given in Table 1, these conditions can be rewritten as

$$f_r \gg \frac{1}{2\pi}\frac{36\eta}{d_c^2\rho_0} \text{and} f_r \gg \frac{1}{2\pi}\frac{16\eta}{\rho_0 r_0^2}. \tag{17}$$

These assumptions mean that that sound propagates in inertial regime through both main perforation and lateral cavities. Third, it is required that porosity of the central perforation wall is much higher than the surface porosity of the sample, $\phi_w \gg \phi_p$. The validity of these approximations for the measured samples will be checked further in the paper.

Now, the following derivation steps are performed. Bessel functions and their combinations are expanded in Taylor series for small arguments $k_cR = O(\varepsilon)$ and $k_cr_0 = O(\varepsilon)$, accounting for terms linear in ε [28]:

$$\begin{aligned} &J_0(k_cr_0) \approx 1 \\ &J_1(k_cr_0) \approx \tfrac{k_cr_0}{2} = O(\varepsilon) \\ &\tfrac{J_1(k_cR)}{H_1(k_cR)}H_0(k_cr_0) \approx -(k_cR)^2\log k_cr_0 = o(\varepsilon) \\ &\tfrac{J_1(k_cr_0)}{H_1(k_cR)}H_1(k_cR) \approx \tfrac{k_cR}{2}\tfrac{R}{r_0} = O(\varepsilon) \end{aligned} \tag{18}$$

These expansions are used to obtain approximation for the second term in the Eq. (6) for the effective compressibility:

$$iC_0\frac{2}{kr_0}\,G_w(\omega) \approx \phi_w C_0\frac{\rho_0 c}{k}\frac{k_c}{Z_c}\left(\left(\frac{R}{r_0}\right)^2 - 1\right) = \frac{(1-\phi_p)\phi_w}{\phi_p}C_c. \tag{19}$$

This results in a simple expression for the effective compressibility $C(\omega)$ of the fluid in the structure

$$C(\omega) \approx C_p + \frac{(1-\phi_p)\phi_w}{\phi_p}C_c, \tag{20}$$

where it is presented as a weighted sum of fluid compressibilities in the main perforation and in the lateral cavities, $C_{p,c}$.

Second, using expressions for JCAL model parameters given in Table 1 and assumption of the inertial regime achieved in the pore and in the cavities at resonance (17) effective compressibilities of air in the perforation and in the lateral cavities, $C_{p,c}$ are approximated as

$$C_{p,c}(\omega) \approx C_0\left(1 + (\gamma-1)\frac{2}{x_{p,c}}\sqrt{\frac{\eta}{-i\omega N_{pr}\rho_0}}\right), \tag{21}$$

where $x_p = r_0$ and $x_c = d_c$. Together with Eq. (20) and approximation of a low porosity ϕ_p, $\phi_w \gg \phi_p$, this leads to the final approximation of $C(\omega)$:

$$C(\omega) \approx C_0\left(1 + \frac{\phi_w}{\phi_p} + \frac{(\gamma-1)}{\sqrt{N_{pr}}}\frac{2}{r_0}\sqrt{\frac{\eta}{-i\omega\rho_0}}\left(1 + \frac{r_0}{d_c}\frac{\phi_w}{\phi_p}\right)\right), \tag{22a}$$

Although $\frac{\phi_w}{\phi_p} \gg 1$ for the designs considered in this work, the first terms in the brackets, are left here to demonstrate that in the absence of the cavities ($\phi_w = 0$), the compressibility of air in the straight cylindrical pore given by Eq. (21) is recovered from Eq. (22a). In the following, however, this term will be neglected transforming (22a) into

$$C(\omega) \approx C_0\frac{\phi_w}{\phi_p}\left(1 + \frac{(\gamma-1)}{\sqrt{N_{pr}}}\frac{2}{r_0}\sqrt{\frac{\eta}{-i\omega\rho_0}}\frac{r_0}{d_c}\right), \tag{22b}$$

In the inertial regime defined by Eq. (17), effective density (5) is approximated as

$$\rho(\omega) \approx \rho_0\left(1 + \frac{2}{r_0}\sqrt{\frac{\eta}{-i\omega\rho_0}}\right). \tag{23}$$

Finally, combining Eqs. (22b) and (23) an approximation for the wavenumber $q(\omega) = \omega\sqrt{\rho(\omega)C(\omega)}$ and characteristic impedance $Z = \sqrt{\rho(\omega)/C(\omega)}$ of air in the pancake absorber are obtained

$$q(\omega) \approx k\sqrt{\frac{\phi_w}{\phi_p}}\left(1 + \frac{1}{r_0}\sqrt{\frac{\eta}{-i\omega\rho_0}}\left(1 + \frac{\gamma-1}{\sqrt{N_{pr}}}\frac{r_0}{d_c}\right)\right). \tag{24a}$$

$$Z(\omega) \approx \rho_0 c\sqrt{\frac{\phi_p}{\phi_w}}\left(1 + \frac{1}{r_0}\sqrt{\frac{\eta}{-i\omega\rho_0}}\left(1 - \frac{\gamma-1}{\sqrt{N_{pr}}}\frac{r_0}{d_c}\right)\right). \tag{24b}$$

Condition of a quarter wavelength resonance for the hard backed structure, $Re(q)L = \frac{\pi}{2}$, leads to a quadratic equation for the square root of the resonance frequency $\sqrt{f_r}$. Its positive solution is

$$\sqrt{f_r} = \frac{\sqrt{f_0}}{2}\left(-\mu + \sqrt{\mu^2 + 4\sqrt{\frac{\phi_p}{\phi_w}}}\right), \tag{25}$$

where

$$\mu = \frac{1}{r_0}\sqrt{\frac{\eta}{-i\omega\rho_0 f_0}}\left(1 + \frac{\gamma-1}{\sqrt{N_{pr}}}\frac{r_0}{d_c}\right) \tag{26}$$

and $f_0 = \frac{c}{4L}$ is the quarter wavelength resonance frequency of air slab of thickness L. Further approximation is made assuming $|\mu^2| \gg 4\sqrt{\frac{\phi_p}{\phi_w}}$, or, roughly,

$$\sqrt{\frac{\phi_p}{\phi_w}} \gg 0.01\ \frac{f_{b\ p}}{f_0} \tag{27}$$

where $f_{b\ p} = \frac{\omega_{b\ p}}{2\pi} = \frac{8\eta}{\pi\rho_0 r_0^2}$ and the characteristic viscous frequency $\omega_{b\,p}$ for the main perforation is given in Table 1.

The validity of this approximation for the experimental designs will be confirmed later. Final estimate for the resonance frequency is

$$f_r \approx f_0\sqrt{\frac{\phi_p}{\phi_w}}\left(1 - \frac{1}{4}\sqrt{\frac{f_{b\ p}}{2f_0}}\sqrt{\frac{\phi_w}{\phi_p}}\left(1 + \frac{\gamma-1}{\sqrt{N_{pr}}}\frac{r_0}{d_c}\right)\right). \tag{28}$$

Under the same assumptions, absorption coefficient at resonance is now estimated. First, we note that at the resonance frequency $qL = \frac{\pi}{2}(i + 1 - \frac{f_r}{f_0}\sqrt{\frac{\phi_w}{\phi_p}})$ and, using Eq. (24b), obtain the following estimation of the normalised surface impedance (12):

$$Z_s \approx \frac{\rho_0 c}{\sqrt{\phi_w\phi_p}}\left(1 + \frac{1}{r_0}\sqrt{\frac{\eta}{-i\omega\rho_0}}\left(1 - \frac{\gamma-1}{\sqrt{N_{pr}}}\frac{r_0}{d_c}\right)\right)\frac{1-e^{-n}}{1+e^{-n}}, \tag{29}$$

where $n \approx \pi(1 - \frac{f_r}{f_0}\sqrt{\frac{\phi_w}{\phi_p}})$. Then, this is substituted into the expression (13) for the absorption coefficient. Since $\sqrt{\phi_w\phi_p} \ll 1$ and $|\frac{1}{r_0}\sqrt{\frac{\eta}{-i\omega\rho_0}}| \ll 1$, their products are neglected. Finally, the following estimation of the absorption coefficient at resonance α_r is obtained

$$\alpha_r \approx \frac{4\sqrt{\phi_w\phi_p}\left(1 - e^{-2n}\right)}{\left(\left(\sqrt{\phi_w\phi_p} + 1\right) - e^{-n}\left(1 - \sqrt{\phi_w\phi_p}\right)\right)^2}. \tag{30}$$

Estimations given by Eqs. (28) and (30) are convenient to investigate the dependence of the resonance frequency and the peak value of the absorption coefficient on the geometry of the structure.

2.2. Experiments and linear model validation

The experiments have been performed on the samples composed of plates with thickness $d_p = 1$ mm and spacings between them $d_c = 1$ mm, 3 mm, 6 mm and plates with thickness $d_p = 3$ mm with spacings $d_c = 1$ mm. The radius of the central perforation was kept $r_0 = 4$ mm and the outer radius of all samples was $R = 50$ mm. This means that for all samples the surface porosity was $\phi_p = 6.4 \times 10^{-3}$.

Table 2
Measured, $f_r^{(1)}$ and $\alpha_r^{(1)}$, predicted by the full model, $f_r^{(2)}$ and $\alpha_r^{(2)}$, and predicted by approximations (28) and (30), $f_r^{(3)}$ and $\alpha_r^{(3)}$,values of the first resonance frequency f_r and peak absorption coefficient α_r for all samples. Dimensions of the samples – columns 2-4, ϵ is relative error between the measured resonance frequency $f_r^{(1)}$ and approximation $f_r^{(3)}$ given by Eq. (28), in %.

Sample	L, mm	d_p, mm	d_c, mm	$f_r^{(1)}$, Hz	$f_r^{(2)}$, Hz	$f_r^{(3)}$, Hz	ϵ, %	$\alpha_r^{(1)}$	$\alpha_r^{(2)}$	$\alpha_r^{(3)}$
1	31	1	1	262	265	270	3	0.87	0.97	0.98
2	30	1	3	229	229	231	1	0.99	0.96	0.96
3	35	1	6	222	187	189	15	0.99	0.92	0.92
4	60	1	1	146	144	144	2	0.88	0.91	0.92
5	58	1	3	135	125	125	7	0.99	1.0	1.0
6	63	1	6	134	108	108	17	1	0.97	0.97
7	33	3	1	337	343	363	8	0.94	0.92	0.94
8	60	3	1	185	202	206	11	0.90	0.86	0.87

The structures are constructed of aluminium alloy for both plates and spacers (thin rings with outer radius equal to R). The thickness of the spacers was 1 mm and the cavities' thickness could be varied depending on the number of spacers used.

Absorption coefficients of the rigidly terminated structures were measured in a standard B&K impedance tube with inner radius 100 mm, using two microphone method. The working range of the apparatus was 50Hz – 1600 Hz. The frequency resolution was 1 Hz. The purpose of these measurements was to provide a variety of data for the comparisons with the model. Fig. 2(a–c) shows comparisons of the impedance tube data for the absorption coefficient with the model based on Eqs. (5), (6), (11), (14), (15) (referred to as "full model" in the following) for samples with thickness close to 30 mm. Corresponding results for samples with thickness close to 60 mm are shown in Fig. 3(a–c). The range of the thicknesses was due to the discrete nature of the material structure and imperfections of the plates and the spacers.

Porosity of the main pore walls due to the presence of the cavities were $\phi_w = 0.5$ for $d_c = 1$ mm, $\phi_w = 0.75$ for $d_c = 3$ mm and $\phi_w = 0.87$ for $d_c = 6$ mm.

In addition to the samples constructed of 1 mm plates, we performed impedance tube measurements on the samples constructed of 3 mm plates with spacings between them equal to 1 mm. The aim of these measurements was to test the model in the case of a relatively low ($\phi_w = 0.25$) porosity of the wall. The results are shown in Fig. 4.

The predictions for Helmholtz resonator absorption coefficient are shown in all figures for comparison. The Helmholtz resonator was modelled as a single plate (plate thickness was kept the same as those of the absorbers) with 8 mm diameter perforation backed by a rigidly backed air cavity. The overall thickness of the resonator was in each case equal to that of the absorber. In calculations for both absorber and Helmholtz resonator the end correction $l_e = \frac{8}{3\pi} r_0$ [29] was accounted for. In case of Helmholtz resonator two end corrections (external and internal) have been added to the thickness of the plate. This is justified by the fact that Helmholtz resonator cavity size was much larger than l_e. For the absorbers only external end correction has been considered.

Table 2 summarizes the results of the measurements for the first absorption peak frequency. Full model predictions and those given by the simplified Eqs. (28) and (30) for the frequency of the first resonance and the peak value of the absorption coefficient. The characteristic frequency for the air in the main pore was the same in all configurations, $f_{b\,p} = 2.5$ Hz, the characteristic frequencies f_{bc} for air in the cavities were $39.2, 9.8\, and\, 2.5$ Hz for $d_c = 1,\ 3$ and 6 mm respectively.

To make sure that the approximations given by Eqs. (28) and (30) can be used, the conditions of their applicability given by Eqs. (16), (17) and (27) were checked and proven valid. The only marginal case is the second of conditions (17) for Sample 4 which results in inequality $39.2 << 146$. However, a good agreement is still observed between the measurements and the predictions for the first resonance peak for this sample. The disagreements between the measurement and the predictions for f_r are the strongest ($\geq$ 15%) for samples 3 and 6 with wider cavities, $d_c = 6$ mm. However, the full and the approximate models give nearly identical predictions for these samples, so the disagreement is observed because the model based on effective properties is only applicable when $r_0 > d_c$. This has been assumed in our previous work [2] when the dead-end pore was described by the surface's impedance $Z_{s\,de}$ for the wave travelling through the main pore and is essential for Eqs. (1)–(3) to be valid. The assumption $r_0 > d_c$ implicitly states the existence of "scale separation" [25] between the main pore and the cavities, and the existence of small parameter $\frac{d_c}{r_0} < 1$. Indeed, by inspecting Eq. (6) it becomes clear, that the modification of the compressibility due to the presence of the side cavities (6) is identical to that predicted for a double porosity material with high permeability contrast, given by Eq. (103) from [25]. The structures we studied could indeed be described as double porosity material with one porosity scale formed by the main pore and another by the side cavities.

Apart from this case, the difference between the predicted and measured values of the first resonance frequency f_r and peak absorption α_r are no more than 11% (Sample 8).

The resonance frequency f_r depends strongly on the porosity of the central pore wall ϕ_w decreasing from 337 Hz for Sample 7 with $\phi_w = 0.25$ to 222 Hz for Sample 3 with $\phi_w = 0.75$ (the samples have close thicknesses of 33 mm and 35 mm respectively). This is the decrease of more than 30%. The measured peak value of the absorption coefficient, however, grows only slightly, from 0.94 for Sample 7 to 0.99 for Sample 3. A similar decrease (29%) in the frequency of the first resonance

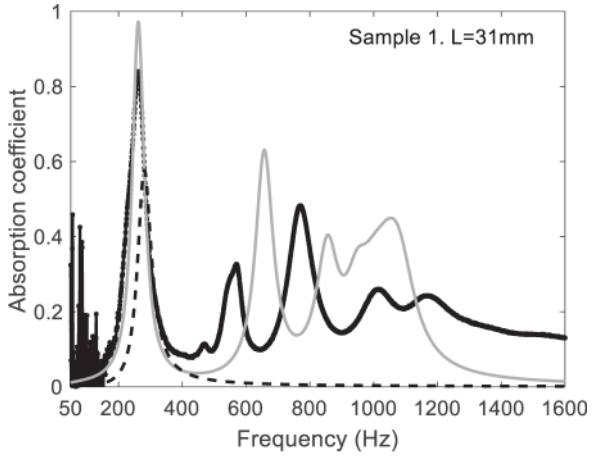

(a)

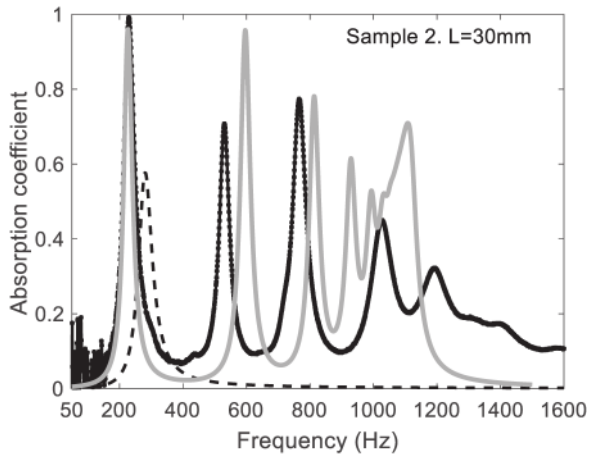

(b)

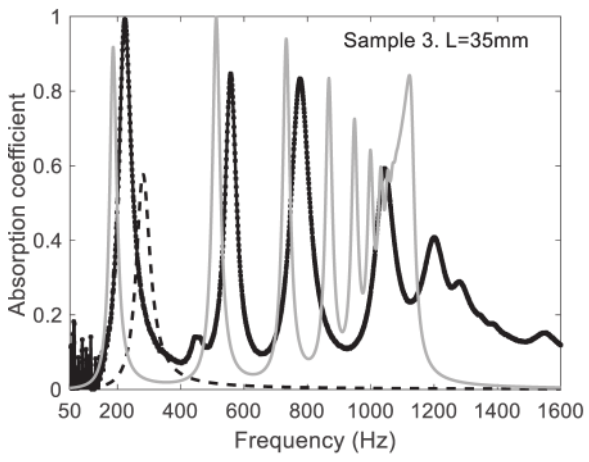

(c)

Fig. 2. Absorption coefficient data (markers) and full model predictions (grey lines) for hard backed absorbers composed of 1 mm thick plates, absorber thickness is around $L = 30$ mm. Spacings between the plates are $d_c = 1$ mm (a), $d_c = 3$ mm (b) and $d_c = 6$ mm (c). Absorption coefficient predictions for Helmholtz resonator of same size as the absorber is shown by dashed lines. Exact thicknesses are given in each figure.

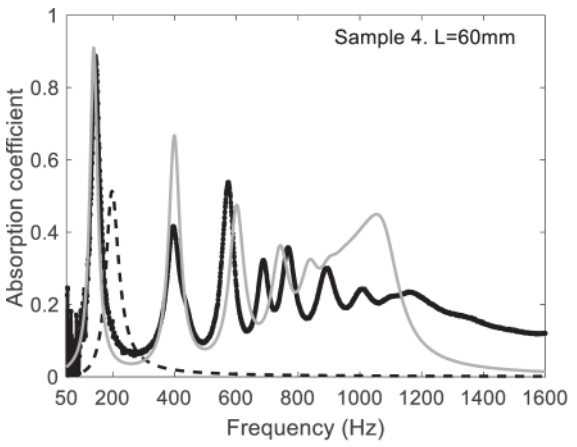

(a)

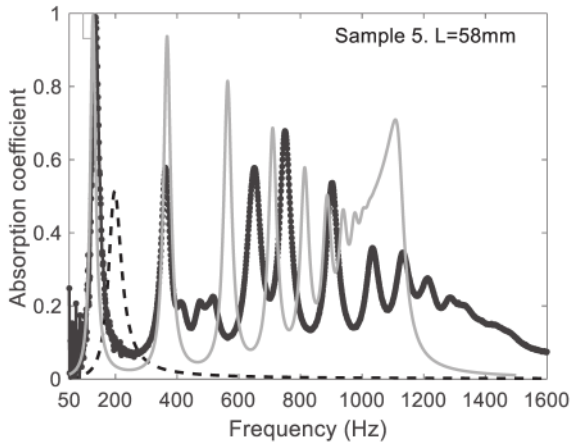

(b)

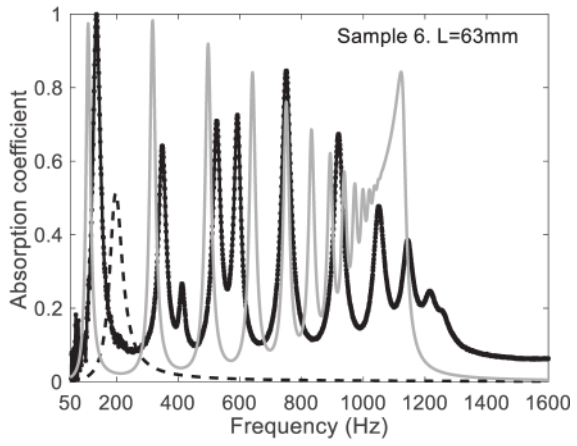

(c)

Fig. 3. Absorption coefficient data (markers) and full model predictions (grey lines) for hard backed absorbers composed of 1 mm thick plates, absorber thickness is around $L = 60$ mm. Spacings between the plates are $d_c = 1$ mm (a), $d_c = 3$ mm (b) and $d_c = 6$ mm (c). Absorption coefficient predictions for Helmholtz resonator of same size as the absorber is shown by dashed lines. Exact thickness value is given in each figure.

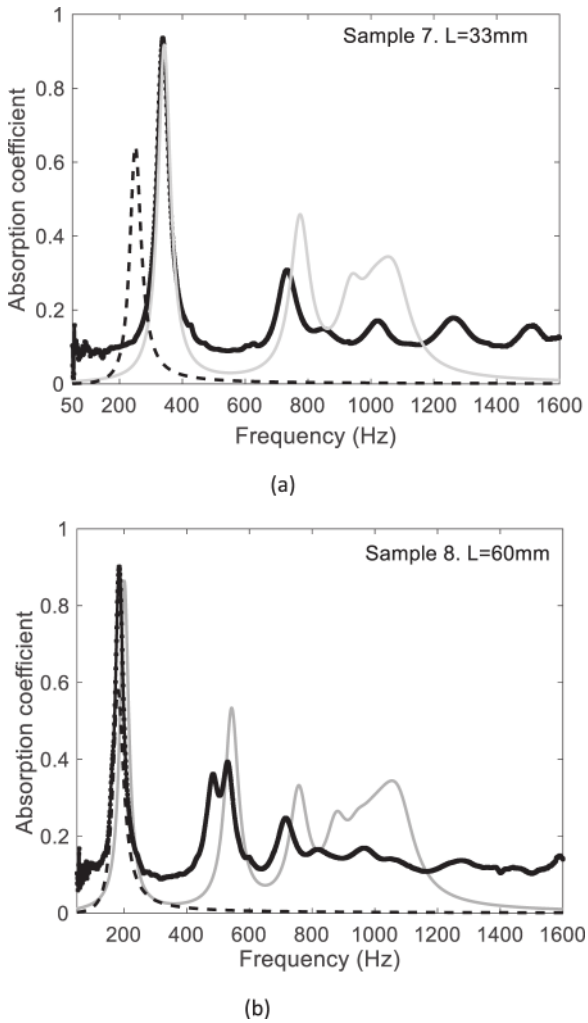

Fig. 4. Absorption coefficient data (markers) and full model predictions (grey lines) for hard backed absorber composed of 3 mm plates with spacings between the plates $d_c = 1$ mm, (a) - absorber thickness $L = 33$ mm, (b) – absorber thickness $L = 60$ mm (b). Absorption coefficient predictions for Helmholtz resonator of same size as the absorber is shown by dashed lines.

is observed for thicker samples, where measured f_r decreases from 185 Hz (Sample 8, thickness 60 mm, $\phi_w = 0.25$) to 131 Hz (Sample 5, thickness 58 mm, $\phi_w = 0.75$). The increase in the measured peak value of the absorption coefficient is more substantial in this case, from 0.9 to 0.99. To illustrate this dependence, the frequency of the first peak and the peak value of the absorption coefficient are plotted against cavity width d_c in Fig. 5a and b respectively for the absorbers with thickness made from the plates with thickness 1mm. The predictions of the full model are close to the approximate expressions (28) and (30) when the cavity width is not too small. In the latter case the characteristic frequency of air in the cavities f_{bc} is no longer small compared to the frequency of the first resonance, so the inertial regime assumed in the derivation of the approximate expressions is no longer valid. The theoretical values are in good agreement with the data for the peak value of the absorption coefficient. For the frequency of the first resonance, the disagreement is more substantial for Sample 5 and 6. The cause for disagreement for Sample 6 is discussed above. Part of the reason for disagreement between the data and the predictions for Sample 5 is the sample thickness which was 58 mm, not 60 mm as assumed in the model. If the comparisons are made for the same sample thicness, the disagreement in the frequency of the first resonance is 7% (see Table 2).

As demonstrated in Figs. 2–4, the first resonance peak of the pancake absorbers is always much higher than that of the Helmholtz resonator when the structures are compared with the same thickness. The resonance frequency f_r is lower for the pancake absorbers than that of the Helmholtz resonator for high pore wall porosity, see data for sample 1–6. However, for sample 7 with low wall porosity, the resonance of the metamaterial structure is observed at higher frequency than that of the Helmholtz resonator. Due to the presence of multiple cavities and coupling between them, multiple absorption peaks are achieved in the low frequency range for the metamaterial absorber when the cavity width exceeds the plate thickness

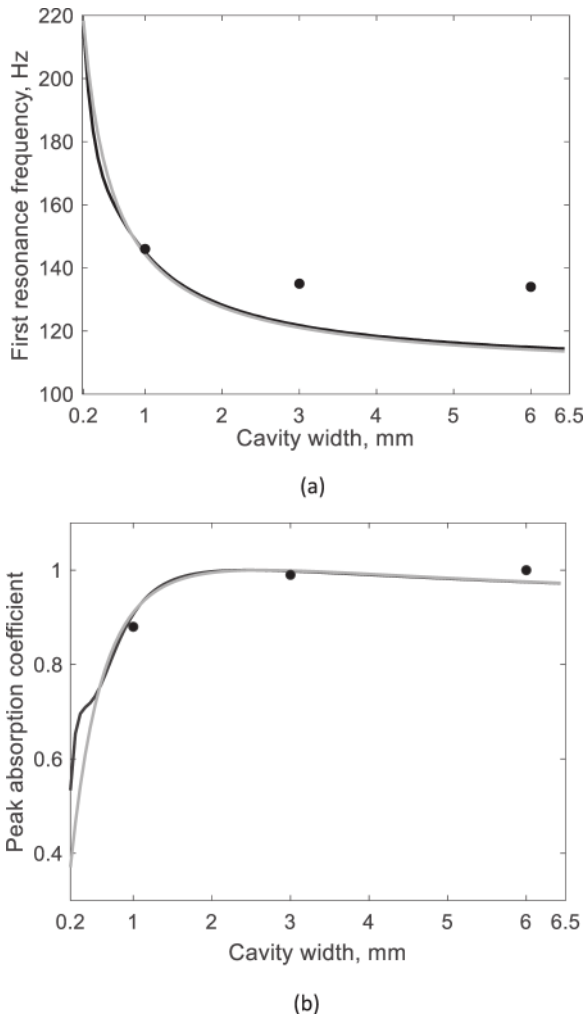

Fig. 5. Measurements (markers), full model predictions (black lines) and approximations given by Eqs. (28) and (30) (gray lines) for different cavity widths. Sample thickness in calculations is 60 mm, plate thickness 1 mm, radius of central perforation is 4 mm. (a) Frequency of the first resonance, (b) Absorption coefficient at resonance.

($d_c > d_p$), as can be seen in Figs. 2c and 3c. This makes metamaterial absorber advantageous over the Helmholtz resonator when multiple frequencies are required to be attenuated.

As follows from Fig. 2–4, the accuracy of the model worsens at higher frequencies, so the predictions of the frequency of the second resonance peak is inaccurate. This is because the assumption $Re(q)h \ll 1$ is only valid at low frequencies. Calculations of the wave speed for the sample with $d_p = 1$mm and $d_c = 3$mm give 46 m/s at 50 Hz decreasing slowly to 29 m/s at 1000 Hz. This means that at $Re(q)h = 0.5$ at 760 Hz and at higher frequencies the model is no longer applicable.

At high frequencies absorption coefficient is low for all samples. This is manifestation of a bandgap occurring due to quarter wavelength resonance of the cavities. Calculations of the wave speed in cavities show that, for the example considered above, this resonance happens around 950 Hz. However, $Re(q)h \approx 1$ at 1000 Hz, so the model predictions in this frequency range are not reliable.

Yet another contribution to discrepancies observed at frequencies higher than the first absorption peak can be explained by the interference of vibrational bandgaps as observed in [1]. According to [30] the first resonance frequency of thin circular plate with radius R and thickness d_p can be calculated as

$$f_{plate} = \frac{\lambda^2 d_p}{2\pi R^2}\sqrt{\frac{E}{12\rho(1-\nu)}}, \tag{31}$$

where E, ν and ρ are Young's modulus, Poisson ratio and density of plate material respectively. The value of constant λ^2 depends on the type of boundary conditions. So, $\lambda^2 = 10.2158$ for clamped circular plate and $\lambda^2 = 4.977$ for simply supported plate. Although the boundary conditions for the plate in the absorber are difficult to identify, we could assume that they

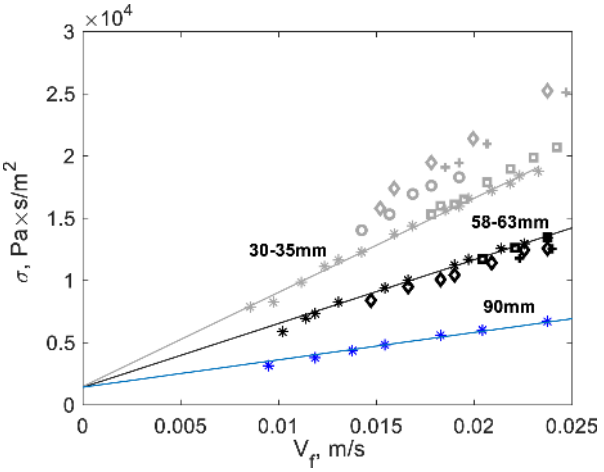

Fig. 6. Flow resistivity of the absorbers and the solid cylinders with central perforation for low flow rates, thicknesses 30–35 mm, 58–63 mm and 90 mm at low flow rates V_f. Stars – solid cylinders with central perforation, squares – 1mm cavities, crosses – 3 mm cavities, circles – 5 mm cavities, diamonds – 6 mm cavities, lines – linear fit for solid cylinders with central perforation.

are between "simply supported" and "clamped". For the aluminum plate with $R = 50$ mm and $d_p = 1$ mm $f_{plate} = 495.9$ Hz for the simply supported plate and $f_{plate} = 1011.6$ Hz for clamped plate. Moreover the material can also be considered as a periodic array of vibrating plate, then a second stop band effect (a vibrational bandgap effect) can occur around the first structural resonance frequency of the plate. This confirms that the plate resonances might contribute to discrepancies between the model and experiments for frequencies higher than the first absorption peak, as observed in Figs. 2 and 3. For thicker plates, the resonance frequencies are higher. However, the disagreement between the model and the measurements for the absorbers comprised of plates with $d_p = 3$ mm is still considerable for frequencies above the first resonance, as shown in Fig. 4. This is apparently due to breaking the low frequency approximation, as explained above.

It could be concluded, that the model developed accurately predicts the absorber behavior at low frequencies. In general, the first absorption peak frequency for the tested absorbers is much higher than that for the corresponding Helmholtz resonator. In addition, the tested structures have several absorption peaks in the frequency range below the bandgap and hence much broader absorption band than the Helmholtz resonators.

3. Flow resistivity measurements and determination of Forchheimer's nonlineariy parameter

Flow resistivity was measured for samples 1-6 (Table 2) to investigate its dependence on the sizes of the lateral cavities. In addition, a 30 mm thick sample with 5 mm cavities, i.e. $d_c = 5$ mm, was constructed and measured. We also measured flow resistivity of three solid cylindrical samples with thicknesses $L = 30,\ 60$ and 90 mm, an outer radius $R = 50$ mm, all having central perforation of radius $r_0 = 4$ mm.

The flow resistivity measurements have been performed at low flow rates in the laminar regime (inside the rig tube) using University of Salford measurement rig described by Turo in [31]. The rig was fitted with a tube having radius 50 mm in order to fit the samples. According to BS EN29053 [32] a flow rate of 0.5 mm/s is recommended, however the lowest we could achieve was 10 mm/s. The static flow resistivity σ_0 has been determined measuring pressure drop along the sample ΔP at several flow rates V_f and using straight line interpolation at zero flow velocity, in accordance with Forchheimer's law [33]

$$\sigma\left(V_f\right) = \frac{\Delta P}{V_f L} = \sigma_0\left(1 + \xi V_f\right) \tag{32}$$

where ξ is Forcheimer's nonlinearity parameter. Static flow resistivity values for low flow rates were measured for all samples in the flow range $V_f \leq 3$ cm/s are shown in Fig. 6. Different markers are used for samples with different cavity widths and solid cylinders with the central perforation, as explained in Fig. 6 caption. Straight lines are the least squares approximations, according to Eq. (32), for solid cylinder samples. The experimental error was estimated around 2.5% and mostly due to inaccuracies of flow rate measurements. This resulted in regression error of intercept (static flow resistivity) and slope (Forchheimer's pameter) of about 10% for most samples.

The values of static flow resistivity σ_0 and Forchheimer's parameter ξ for all measured samples are given in Table 3. The theoretical value for the straight cylindrical pore with $r_0 = 4$mm calculated using expression given in Table 1 is 1405 $\frac{\text{Pa·s}}{\text{m}^2}$. The values of static flow resistivity σ_0 for all measured samples were close (within 10% error margin) to that theoretical value, indicating weak influence of the cavities in $V_f \to 0$ limit. The thickness of the sample has little influence on σ_0.

Table 3
Measured static flow resistivity σ_0 and Forchheimer's parameter ξ for all samples.

L, mm	d_p, mm	d_c, mm	σ_0, $\frac{\text{Pa s}}{\text{m}^2}$	ξ, $\frac{\text{s}}{\text{m}}$
31	1	1	1482.5	529.8
30	1	3	1471.2	642.6
30	1	5	1505.9	592.1
35	1	6	1414.5	710.6
30	Circular	orifice	1481.0	511.1
60	1	1	1422.5	360.2
58	1	3	1541.6	297.8
63	1	6	1456.2	327.1
60	Circular	orifice	1449.4	346.9
90	Circular	orifice	1425.8	154.4

The weak dependence of the static flow resistivity on the presence of the cavities confirms the high permeability contrast between the two porosity scales mentioned in Section 2.3 and the use of Eq. (5) for the effective density.

Forchheimer's parameter values for our samples are much higher than those measured before for conventional porous materials. For instance, the Forchheimer's parameter value for lead shot and gravel reported in [13] were 3.70 s/m and 4.06 s/m and did not depend on the thickness of the sample. Some values we measured are two orders of magnitude higher than that. This difference is due to a very low surface porosity $\phi_p = 6.4 \times 10^{-3}$ of our samples and hence high flow velocity inside the perforation $U = \frac{V_f}{\phi_p}$ and the large pore scale Reynolds number $Re = \frac{2r_0 U \rho_0}{\eta} = \frac{2r_0 V_f \rho_0}{\phi_p \eta}$ achieved even at moderate flow rates V_f inside the rig. In fact, for $V_f = 0.01 \frac{\text{m}}{\text{s}}$, pore scale Reynold's number is $Re = 829$. For the samples with close thickness, measured values of Forchheimer's parameters are also close to each other. However, a clear trend was observed, that Forchheimer's parameter values are higher for thinner samples. For samples with the thickness in the range $30 - 35$ mm, the range of Forchheimer's parameter values is $511.1 - 710.6 \frac{\text{s}}{\text{m}}$. For those with thickness $58 - 63$ mm, Forchheimer's parameter range is $297.8 - 360.2 \frac{\text{s}}{\text{m}}$. And, finally, for the sample with thickness $L = 90$ mm, measured Forchheimer's parameter is $154.4 \frac{\text{s}}{\text{m}}$.

The dependence of the Forchheimer's parameter on the thickness of the sample could be explained empirically, if we consider the extra losses at the entrance and the exit of the sample as suggested by Astarita and Greco [34] and Oliveira and Pinho [35]. Following [34], the pressure drop through the sample $\Delta P = p_{ent} - P_0$, where p_{ent} and P_0 are pressure values some distance upstream and downstream of the sample, where the end effects are negligible, could be decomposed in the following way $\Delta P = (p_{ent} - p_a) + (p_a - p_b) + (p_b - P_0)$. Here p_a and p_b are pressure at the positions a and b inside the pore, where the flow is fully developed. The excess pressure drops $\Delta p_1 = p_{ent} - p_a$ and $\Delta p_2 = p_b - P_0$ are due to sudden changes in the tube aperture at the entrance and the exit of the sample. They consist of the reversible pressure decrease and increase attributable to Bernoulli effects due to change in velocity. As $\phi_p \ll 1$, it can be assumed that the net effect of these pressure drops is zero. There are also irreversible pressure drops which happen when the fluid accelerates and decelerates creating recirculation zone [35]. For large Reynolds numbers the main contribution to these pressure drops is proportional to V_f^2, (see Fig. 9a in [35] and Fig. 4 in [34], so that the combined effect can be described as $(p_{ent} - p_a) + (p_b - P_0) = AV_f^2$, where A is some coefficient.

This means that the contributions of the end effects to the measured flow resistivity value could be approximated as:

$$\sigma\left(V_f\right) = \frac{\Delta P}{V_f L} \approx \frac{AV_f}{L} + \sigma_{tube}\left(V_f\right) \tag{32'}$$

where $\sigma_{tube}(V_f) = \frac{(p_a - p_b)}{V_f L}$ is the flow resistivity value in case of infinite tube and no end effects and $\frac{AV_f}{L}$ is the contribution of the extra losses occurring in the regions of sudden contraction and sudden expansion. Comparisons between (32) and (32') allow us to conclude that the excess pressure drops in the flow through sudden contraction and expansion contributes to the gradient of $\sigma(V_f)$, i.e. Forchheimer's parameter. Moreover, the appearance of the sample thickness L in denominator of the first term in (32') explains the stronger influence of the end effects on the Forchheimer's parameter value of shorter samples.

A similar trend, showing higher flow resistivity values and higher $\sigma(V_f)$ gradients for shorter samples, is observed for higher flow rates. Fig. 7, a shows flow resistivity dependence on the flow rate for $0.05 \frac{\text{m}}{\text{s}} \leq V_f \leq 0.25 \frac{\text{m}}{\text{s}}$ (pore scale Reynolds number range $4000 \leq Re \leq 20718$) for samples 1, 2 and 4, 5 from Table 2. According to Landau and Lifshitz [36], p.177 this corresponds to turbulent flow regime of air in the pore. Flow resistivity of samples 1 and 4 with thicknesses close to 30 mm are much higher than those of 2 and 5 with thicknesses close to 60 mm in the whole range of flow rates. Alongside with the measured results, predictions of flow resistivity $\sigma_{tube}(V_f)$ in the turbulent regime is plotted. It is given in the implicit

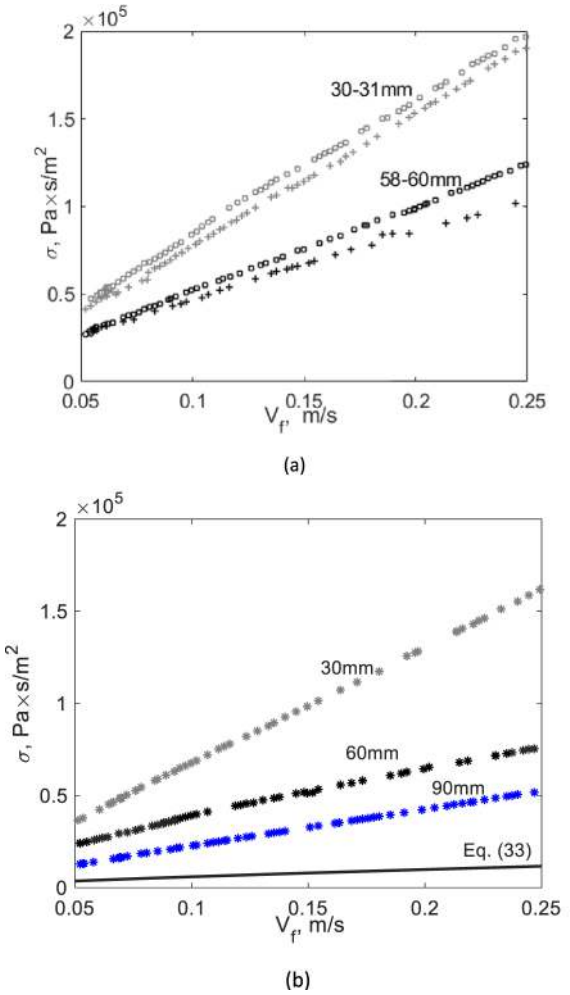

Fig. 7. Flow resistivity of the absorbers (a) and solid cylinders with the central perforation (b) for high flow rates. Crosses – 3 mm cavities, squares - 1 mm cavities, stars – solid cylinders with central perforation, line – flow resistivity of the tube as predicted by Eq. (33).

form by Eqs. (43.4) and (43.5) from [36]. These equations were combined to give dependence $\sigma_{tube}(V_f)$ as

$$\sigma_{tube}(V_f) = \frac{\rho_0 V_f}{4 r_0 \phi_p^2}\left(0.44 \ln\left(\frac{16 r_0^3 \rho_0 V_f}{\eta^2}\sigma_{tube}(V_f)\right) - 0.85\right)^{-2}. \tag{33}$$

This equation does not account for any end effects and considers losses within the pore only. In Fig. 7b these results are compared with the data for flow resistivity of three cylinders with the central perforation, with thickness 30 mm, 60 mm and 90 mm. For thicker samples the flow resistivity is lower, staying however much higher than predictions of Eq. (33), presumably due to the end effects. It is also noted by comparing Fig. 7a and b, that for the high flow rates, the flow resistivity of the absorbers is significantly higher than that of the cylinders with central perforation. This means, that although the presence of cavities has little effect on the flow resistivity measured at conventional i.e. low flow rates (Fig. 6), this is not the case for high flow rates. However, there is relatively little difference between the data for samples with 1mm and 3 mm cavities (squares and crosses in Fig. 7a) and this difference is more noticeable for longer samples. This is to be expected as the contribution of end effects to flow resistivity values is stronger for shorter samples (see Eq. (32')) and hence the difference in flow conditions within the central pore is masked.

4. Absorber in the nonlinear regime – model and its experimental validation

4.1. Model

Here we follow an approach adopted in previous studies of porous absorbers' interactions with high amplitude sound, see for example [6,10,13]. This means, that the only source of nonlinearity is the empirically introduced dependence of flow

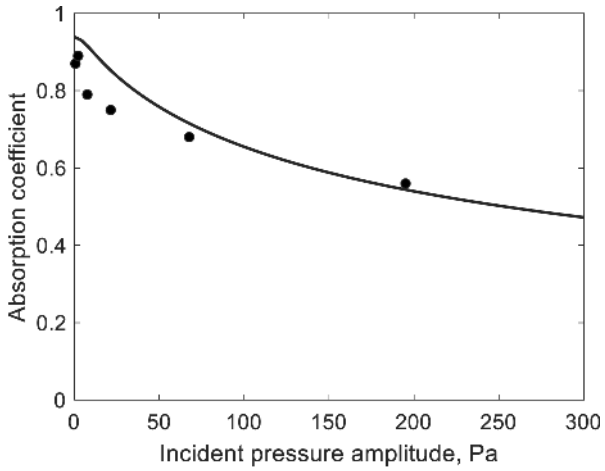

(a)

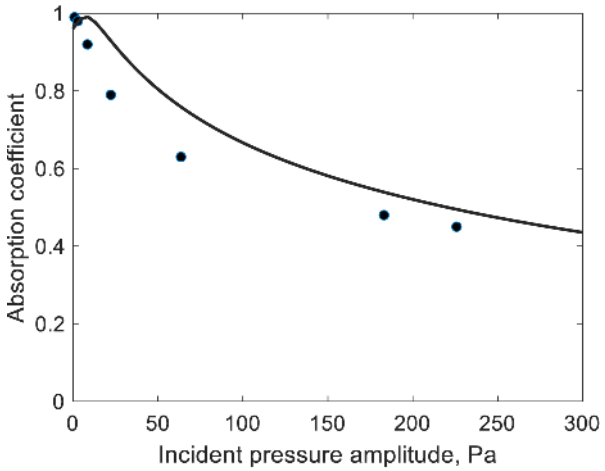

(b)

Fig. 8. Measurements (markers) and nonlinear model (Eqs. (37), (38) and (43), (44)) predictions (lines) for the first absorption coefficient peak variations with incident pressure amplitude. (a) Sample 1, thickness 31 mm (b) Sample 2, thickness 30 mm. Measurement points are shown for experimental peak frequencies $f_r^{(1)}$, while numerical results are shown for frequencies $f_r^{(2)}$ predicted by the model, given in Table 2. Sample dimensions are given in Table 2.

resistivity of particle velocity v of sound in the pores, $\sigma(v)$. In previous studies, this dependence is approximated by the linear relationship $\sigma(v) = \sigma_0(1 + \xi\phi_p|v|)$, which is similar to (32) with $V_f = \phi_p v$. It was also postulated that the parameter of nonlinearity, ξ, can be measured in static flow resistivity tests. However, the characteristic feature of our samples is that the Forchheimer's parameter depends on the thickness of the sample and on the size of the cavities. For this reason, in the model a measured dependence of the flow resistivity on flow velocity $\sigma(\phi_p|v|)$ was used, for each sample, instead of a single linear approximation. This was combined with Eqs. (5) and (14) to result in the following particle velocity dependent effective density of fluid in the pore ($\alpha_{\infty\ p} = 1$)

$$\rho(\omega,\ v) = \rho_0 \left(1 + \frac{\sigma(\phi_p|v|)}{-i\omega\rho_0} \sqrt{1 + \frac{-4i\omega\rho_0\eta}{\Lambda^2\sigma(\phi_p|v|)^2}}\right). \tag{34}$$

It was shown in the previous section, that for low intensity sound, the inertial regime approximation $\omega \gg \omega_{b\,p}$ is valid around the frequency of the first resonance. In the nonlinear regime this assumption is no longer valid as the frequency $\omega_{b\,p}$ has a quadratic dependence on flow resistivity, $\omega_{b\ p} = \frac{\sigma(\phi_p|v|)^2\Lambda^2}{4\rho_0\eta}$, and consequently could attain very high values at high amplitudes. Assuming harmonic excitation, we start with the usual momentum and mass conservation equations for the equivalent fluid saturated the material

$$-i\omega\rho(\omega, v)v = -\frac{\partial p}{\partial x}, \tag{35}$$

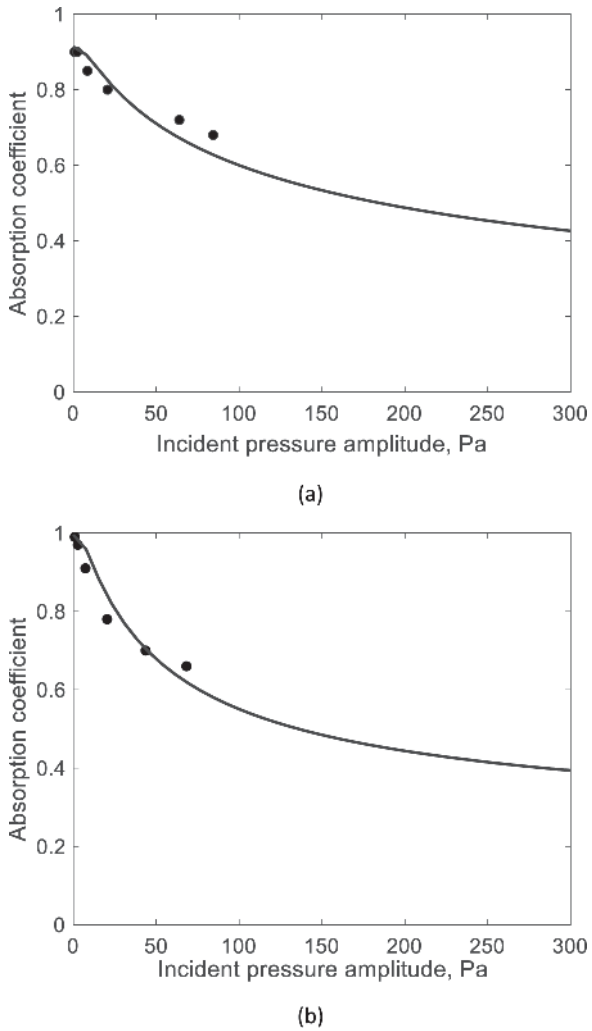

Fig. 9. Measurements (markers) and nonlinear model (Eqs. (37), (38) and (43), (44)) predictions (lines) for the first absorption coefficient peak variations with incident pressure amplitude. (a) Sample 4 thickness 60 mm (b) Sample 5, thickness 58 mm. Measurement points are shown for experimental peak frequencies $f_r^{(1)}$, while numerical results are shown for frequencies $f_r^{(2)}$ predicted by the model, given in Table 2. Sample dimensions are given in Table 2.

$$-i\omega C(\omega)v = -\frac{\partial v}{\partial x}. \tag{36}$$

Effective compressibility $C(\omega)$ remains unaffected by the nonlinearity and is defined by Eq. (6). The aim now is to derive equations which eventually enable us to get the dependence of the surface admittance of the sample as a function of the incident wave pressure amplitude p_i. This approach is similar to that used in [6] and [10]. First, we introduce a dimensionless spatial variable $X = \frac{x}{L}$, where L is the thickness of the sample. This way, the surface of the sample corresponds to $X = 0$ and its backing to $X = 1$. Then the equations for the normalised impedance $Z(X) = \frac{1}{\rho_0 c}\frac{p(X)}{v(X)}$ and the normalised particle velocity $V(X) = v(X)\frac{\rho_0 c}{p_i}$, are derived

$$Z' = +ikL\left(\bar{\rho}\left(\omega, V, \xi\frac{p_i}{\rho_0 c}\right) - \bar{C}(\omega)Z^2\right), \tag{37}$$

$$V' = ikL\,\bar{C}(\omega)VZ. \tag{38}$$

Here

$$\bar{C}(\omega) = \frac{C(\omega)}{C_0}, \tag{39}$$

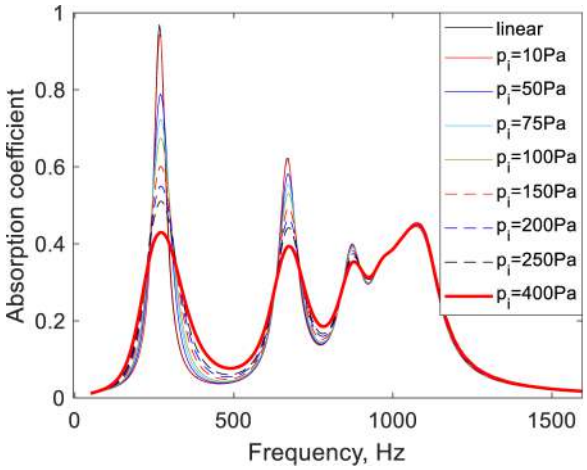

Fig. 10. Model predictions for the absorption coefficent dependence on frequency at different values of incident presure amplitude p_i. Sample 1.

$$\bar{\rho}\left(\omega, V, \xi \frac{p_i}{\rho_0 c}\right) = \frac{\rho\left(\omega, V, \xi \frac{p_i}{\rho_0 c}\right)}{\rho_0} = 1 + \frac{\sigma\left(\phi_p \frac{p_i}{\rho_0 c}|V|\right)}{-i\omega\rho_0} \sqrt{1 + \frac{-4i\omega\rho_0\eta}{\sigma^2\left(\phi_p \frac{p_i}{\rho_0 c}|V|\right)\Lambda^2}}. \tag{40}$$

Prime stands for the derivative with respect to X. The Riccati Eq. (37) for $Z(X)$ is similar to Eq. (20) from [6], while the scaling function for $\bar{\rho}(\omega, V, \xi \frac{p_i}{\rho_0 c})$ resulting from (34) is different from their Eq. (18).

The boundary conditions relating particle velocity v and the admittance G at the surface of the sample $X = 0$ is derived from the conditions of velocity and pressure continuity i.e

$$1 - \frac{p_r}{p_i} = \phi_p V(0), \tag{41}$$

$$1 + \frac{p_r}{p_i} = V(0)Z(0). \tag{42}$$

Eliminating reflected pressure amplitude p_r, the dependence of particle velocity $v(0)$ and the normalised surface impedance of fluid in the pore $Z(0)$ on the incident pressure amplitude p_i is obtained

$$V(0) = \frac{2}{\phi_p + Z(0)}. \tag{43}$$

The second boundary condition is applied at the hard backing of the sample

$$V(1) = 0. \tag{44}$$

Hence, the surface impedance $\frac{Z(0)}{\phi_p}$ of the sample and consequently its absorption coefficient could be found from the solution of Eqs. (37) and (38) with boundary conditions (43) and (44). These values depend on the amplitude of the incident pressure p_i, as it determines the strength of nonlinearity present in Eq. (37). If $p_i = 0$, the solution of the linear model obtained in the previous sections can be recovered.

The equations are solved numerically using the following method. First, the analytical solutions of Eqs. (37) and (38) with boundary conditions (43) and (44), $V_1(X)$ and $Z_1(X)$ are found, assuming $p_i = 0$ and hence no nonlinearity. Then, $V_1(X)$ is substituted in Eq. (37) and the next iteration of the impedance, $Z_2(X)$ is obtained by numerically solving this equation with boundary condition (43) in the form $Z_2(0) = \frac{2}{V_1(0)} - \phi_p$. $Z_2(X)$, in turn, is substituted in Eq. (38), which is solved numerically to obtain $V_2(X)$, with boundary condition (44) $V_2(1) = 0$. The procedure is repeated and stopped only when the difference between two successive iterations of the absorption coefficient is less than 5% in the whole range of p_i values. In the measured frequency range and for $p_i \leq 250250$ Pa, 15 or less iterations is enough to achieve the required accuracy.

4.2. Experiments and model validation

The measurements for high amplitude sound have been performed using a specially designed impedance tube at the ISAT, University of Burgundy, France. Sine wave excitation has been used for a better control over the amplitude of the incident wave. For the usual white noise excitation, there is no guarantee that each frequency component has the same amplitude. The measurements have been performed at the frequency of the absorption coefficient peaks for samples 1, 2, 4 and 5 (Table 1). To obtain the dependence of the peak absorption coefficent on the amplitude of incident wave, the following

procedure has been followed. The surface impedance measurements have been performed for each voltage applied. Two microphone method has been used with the microphones positioned at the distances 100 mm and 150 mm in front of the sample. Additionally, the amplitude of pressure $|p| = P_i(e^{-ikd_0} + Re^{ikd_0})$ has been measured at the distance $d_0 = 50$ mm in front of the sample. The value of the reflection coefficient R has been calculated from the measured surface impedance and then incident pressure amplitude has been calculated as $p_i = \frac{|p|}{e^{-ikd_0}+Re^{ikd_0}}$ for each measurements. For Samples 1 and 2 the measurements have been performed for p_i values in the range of up to 300 Pa. However, for longer samples the range of measured p_i was lower due to limitations of the equipment.

The comparisons between the measured and predicted by nonlinear model dependence of the absorption coefficient at the first peak are shown in Fig. 8a, b for Samples 1 and 2 and in Fig. 9a, b for Samples 4 and 5. It should be noted, that the comparisons have been performed at peak frequencies according to measurements and predictions for low amplitude data, shown in Table 2. For instance for Sample 5, the data points shown in Fig. 8b correspond to frequency $f_r^{(1)} = 135$ Hz, while model predictions have been calculated for predicted peak frequency $f_r^{(2)} = 125$ Hz

To illustrate how the increase of the incident wave amplitude affects the overall shape of the absorption curve, equations have been solved for different frequencies assuming that each frequency component has the same amplitude for $p_i = 0.01$ Pa (linear case) and several increasing values up to $p_i = 400$ Pa. The results are shown in Fig. 10 for Sample 1. The effect of nonlinearity does not significantly change the frequency of the first resonance, while the peak absorption coefficient values are strongly decreased.

5. Conclusions

An absorbing structure comprising of periodically arranged metallic plates separated by air cavities and with a central perforation traversing the periodic structure, was built and tested in both linear and nonlinear regimes.

New models for the linear and the nonlinear acoustic behaviours of this structure were proposed, together with absorption coefficient measurements in the linear regime, flow resistivity and Forcheimer nonlinearity parameter measurements at high flow rates and finally absorption coefficient measurements in the nonlinear regime.

The results of measurements were compared with the models – the analytical linear model and a numerical model accounting for Forchheimer's type nonlinearity.

A good agreement was demonstrated between the model and the absorption coefficient data in the linear regime, i.e. for low levels of the incident sound, and at low frequencies. Simple expressions have been derived that adequately describe the frequency of the first peak and the peak absorption coefficient value.

With carefull choice of parameters for this absorbing structure, an absorption peak at much lower frequency and higher peak value than that provided by a Helmholtz resonator of same thickness and diameter could be achieved. Furthermore, this absorber can provide higher frequency absorption peaks and a broader absorption range.

Flow resistivity measurements for a range of flow velocities were carried out for the absorbers. Typical value of the Forcheimer non linearity parameter were obtained, which is high relative to porous and granular materials so that strong nonlinear effects could be expected for the absorber.

A dependence of flow resistivity on the sample thickness for high flow rates was observed with higher values achieved for shorter samples. A qualitative explanation was given for this behaviour. In the nonlinear model, a measured value of Forcheimer parameter was used for each absorber sample.

It was shown that the absorption peak frequencies weakly depend on the incident pressure amplitude, while the peak values are strongly attenuated as incident pressure grows. This means, that the linear model will overestimate the absorption capacity of the structure, if the latter is used for high sound pressure levels. The new numerical model accounting for Forchheimer's nonlinearity adequately describes the effects observed.

The results of this work will be useful when designing absorbers of tonal sounds for applications in the environments where high sound pressure levels are achieved. Future work will concentrate on the optimum design of the pancake structure allowing perfect absorption at the desired frequency or frequencies. Reducing the number of interstitial walls inside the pancake absorber will eventually lead to Helmholtz resonator while doing the opposite will lead to a quarter wavelength circular cavity. The resonance frequencies associated with these structures are well known. The first resonance frequency of the pancake absorber is lower than that of the Helmholtz resonator (not between that of the Helmholtz and that of the quarter wavelength cavity as expected). This means that the resonance frequency experiences a minimum depending on the number of interstitial walls. This observation shows the importance of optimizing the number of cavities and their sizes in the pancake structure.

Declaration of Competing Interest

The authors declare that they have no known competing financial interests or personal relationships that could have appeared to influence the work reported in this paper.

CRediT authorship contribution statement

Daniel C. Brooke: Conceptualization, Investigation, Methodology, Writing - original draft. **Olga Umnova:** Conceptualization, Methodology, Formal analysis, Supervision, Writing - original draft. **Philippe Leclaire:** Conceptualization, Supervision, Writing - original draft. **Thomas Dupont:** Methodology, Formal analysis, Writing - original draft.

Acknowledgement

The work was supported by DSTL UK through Anglo – French PhD Scheme.

References

[1] T. Dupont, P. Leclaire, R. Panneton, O. Umnova, A microstructure material design for low frequency sound absorption, Appl Acoust 136 (2018) 86–93.
[2] P. Leclaire, O. Umnova, T. Dupont, R. Panneton, Acoustical properties of air-saturated porous material with periodically distributed dead-end pores, J Acoust Soc Am 137 (2015) 1772–1782.
[3] J.P. Groby, W. Huang, A. Lardeau, Y. Auregan, The use of slow waves to design simple sound absorbing materials, J Appl Phys 117 (2014) 124903.
[4] S. Park, A Design method of micro-perforated panel absorber at high sound pressure environment in launcher fairings, J Sound Vib 332 (2012) 521–535.
[5] H.L. Kuntz, D.T. Blackstock, 'Attenuation of intense sinusoidal waves in air-saturated, bulk porous materials, J Acoust Soc Am 81 (1987) 1723–1731.
[6] D.K. Wilson, J.D. McIntosh, R.F. Lambert, Forchheimer-type nonlinearity for high intensity propagation of pure tones in air—saturated porous media, J Acoust Soc Am 84 (1988) 350–359.
[7] J.D. McIntosh, R.F. Lambert, Nonlinear wave propagation through rigid porous materials. I. Nonlinear parametrization and numerical solutions,, J Acoust Soc Am 88 (1990) 1939–1949.
[8] R.F. Lambert, J.D. McIntosh, Nonlinear wave propagation through rigid porous materials. II. Approximate analytical solutions, J Acoust Soc Am 88 (1990) 1950–1959.
[9] Y. Auregan, M. Pachebat, 'Measurement of the nonlinear behaviour of acoustical rigid porous materials, Phys Fluids 11 (1999) 1342–1345.
[10] O. Umnova, K. Attenborough, E. Stanley, A. Cummings, Behaviour of rigid-porous layers at high levels of continuous acoustic excitation: theory and experiment, J Acoust Soc Am 114 (2003) 1346–1356.
[11] O. Umnova, K. Attenborough, H.- Ch. Shin, A. Cummings, Response of multiple rigid porous layers to high levels of continuous acoustic excitation, J Acoust Soc Am 116 (2004) 703–712.
[12] B. Zhang, T. Chen, Y. Zhao, W. Zhang, J. Zhu, Numerical and analytical solutions for sound propagation and absorption in porous media at high sound pressure levels, J Acoust Soc Am 132 (2012) 1436–1449.
[13] O.Umnova D.Turo, Influence of Forchheimer's nonlinearity and transient effects on pulse propagation in air saturated rigid granular materials, J Acoust Soc Am 134 (2013) 4763–4774.
[14] L.J. Sivian, Acoustic impedance of small orifices, J Acoust Soc Am 7 (1935) 94–101.
[15] U. Ingard, H. Ising, Acoustic nonlinearity of an orifice, J Acoust Soc Am 42 (1967) 6–17.
[16] A. Cummings, W. Eversham, High amplitude acoustic transmission through duct terminations: theory, J Sound Vib 91 (1983) 503–518.
[17] A. Cummings, Acoustic nonlinearities and power losses at orifices, AIAA J 22 (1984) 786–792.
[18] V. Achilleos, O. Richoux, G. Theocaris, Coherent perfect absorption induced by nonlinearity of a Helmholtz resonator, J Acoust Soc Am 140 (2016) EL94.
[19] D.Y. Maa, Microperforated panel at high sound intensity, Internoise, Yokohama, Japan, 1994.
[20] R. Tayong, T. Dupont, P. Leclaire, On the variations of acoustic absorption peak with particle velocity in micro – perforated panels at high levels of excitaion, J Acoust Soc Am 127 (2010) 2875–2882.
[21] R. Tayong, T. Dupont, P. Leclaire, Experimental investigation of holes interaction effect on the sound absorption coefficient of micro - perforated panels under high and medium levels, J Appl Acoust 72 (2011) 777–784.
[22] D.L. Johnson, J. Koplik, R. Dashen, Theory of dynamic permeability and tortuosity in fluid – saturated porous media, J Fluid Mech 176 (1987) 379–402.
[23] Z. Laly, N. Atalla, S.- A. Meslioui, Acoustical modelling of micro – perforated panel at high sound pressure levels using equivalent fluid approach, J Sound Vib 427 (2018) 134–158.
[24] N. Atalla, F. Sgard, Modelling of perforated plates and screens using rigid frame porous models, J Sound Vib 303 (2007) 195–208.
[25] X. Olny, C. Boutin, Acoustic wave propagation in double porosity media, J Acoust Soc Am 114 (2003) 73–89.
[26] Y. Champoux, J.F. Allard, Dynamic tortuosity and bulk modulus in air saturated porous media, J Appl Phys 70 (1991) 1975–1979.
[27] D. Lafarge, P. Lemariner, J.F. Allard, V. Tarnow, Dynamic compressibility of air saturated porous structures at audible frequencies, J Acoust Soc Am 102 (1997) 1995–2006.
[28] M. Abramowitz, I.A. Stegun, in: Handbook of mathematical functions, National Bureau of Standards, Washington D. C., 1970, p. 360. eqs. 9.1.10-9.1.11.
[29] L.E. Kinsler, A.R. Frey, A.B. Coppens, J.V. Sanders, in: Fundamentals of Acoustics, Wiley, New York, 2000, p. 274.
[30] A.W. Leissa, in: Vibrations of plates", scientific and information division, NASA, Washington, 1969, pp. 8–9.
[31] D. Turo, A relaxation approach for time domain modelling of sound propagation in porous media PhD thesis, University of Salford, UK, 2011.
[32] BS EN 29053:1993, ISO 9053:1991 "Acoustics. Materials for acoustical applications. Determination of airflow resistance".
[33] P.H. Forchheimer, Wasserbewegung durch Boden, Z Ver Dtsch Ing 45 (1901) 1782–1788.
[34] G. Astavita, G. Greco, Excess pressure drop in laminar flow through sudden contraction. Newtonian liquids, Ind Eng Chem 7 (1968) 27–31.
[35] P.J. Oliveira, F.T. Pinho, Pressure drop coefficient of laminar Newtonian flow in axisymmetric sudden expansions, Int J Heat Fluid Flow 18 (1997) 518–529.
[36] L.D. Landau, E.M. Lifshitz, in: Fluid mechanics, Oxford, Pergamon, 1987, pp. 176–178. §43.